*buildings*

MDPI

*Article*

# Size and Geometry Effects on Compressive Failure of Laminated Bamboo: A Combined Experimental and Multi-Model Theoretical Approach

**Jian-Nan Li [1,*], Amardeep Singh [1,2,*], Jun-Wen Zhou [1], Hai-Tian Zhang [1] and Yun-Chuan Lu [1]**

[1] School of Civil Engineering and Architecture, Changzhou Institute of Technology, Changzhou 213032, China; zhoujw@czu.cn (J.-W.Z.); 23040230@czu.cn (H.-T.Z.); 23040115@czu.cn (Y.-C.L.)
[2] School of Engineering, Design and Built Environment, Western Sydney University, Penrith, NSW 275l, Australia
* Correspondence: lijn@czu.cn (J.-N.L.); adsingh@czu.cn (A.S.)

**Abstract**

Laminated bamboo (LB) represents a promising sustainable construction material, inheriting bamboo's high strength, lightweight properties, and good ductility. However, the dimensional stability of mechanical performance—specifically size effects—remains a critical design challenge requiring systematic investigation. This study investigates the compression behavior of LB with tests of four specimen groups spanning volumes from 62,500 to 4,000,000 mm$^3$ (25 × 25 × 100 mm to 100 × 100 × 400 mm). The research objectives encompass (i) characterizing compression behavior and failure mechanisms across different specimen scales, (ii) quantifying geometric and volumetric size effects on mechanical properties, (iii) evaluating theoretical frameworks for size effect prediction, (iv) developing progressive modeling approaches incorporating material heterogeneity, and (v) establishing design parameters for practical applications. Results demonstrate modest proportional size effects (1.60% strength reduction, 8.62% modulus reduction for 4× proportional scaling) but significant geometric optimization benefits, with cubic specimens achieving 15.78% higher strength and 25.11% greater modulus than equivalent-volume prismatic specimens. All specimens exhibited interfacial delamination failure with size-dependent crack propagation patterns. Theoretical analysis incorporates Weibull statistics, Bažant's fracture mechanics, and Carpinteri's fractal theory, with fracture energy modeling performing optimally. Three progressive modeling approaches achieve prediction accuracies ranging from 1.17% to 0.37% errors, with density-coupled modeling providing superior performance despite minimal density variations (COV = 9.27%). The research establishes size effect factors (0.86 for strength, 0.78 for modulus) and critical dimensions (125.64–126.14 mm), addressing critical gaps in LB size-dependent behavior. These parameters enable the development of reliable design methodologies for large-scale sustainable construction.

**Keywords:** engineered bamboo; dimensional effects; mechanical characterization; failure analysis; predictive modeling; density-coupled analysis

check for updates

Received: 20 August 2025
Revised: 5 September 2025
Accepted: 8 September 2025
Published: 9 September 2025

**Citation:** Li, J.-N.; Singh, A.; Zhou, J.-W.; Zhang, H.-T.; Lu, Y.-C. Size and Geometry Effects on Compressive Failure of Laminated Bamboo: A Combined Experimental and Multi-Model Theoretical Approach. *Buildings* **2025**, *15*, 3261. https://doi.org/10.3390/buildings15183261

**Copyright:** © 2025 by the authors. Licensee MDPI, Basel, Switzerland. This article is an open access article distributed under the terms and conditions of the Creative Commons Attribution (CC BY) license (https://creativecommons.org/licenses/by/4.0/).

## 1. Introduction

The construction industry faces pressing challenges in developing sustainable and reusable materials, particularly as global environmental concerns and resource scarcity intensify. Traditional reinforced concrete, while ubiquitous, presents significant limitations in addressing these sustainability imperatives. This has catalyzed the development of

alternative materials, including 3D-printed layered concrete and bio-based composites [1–3]. Among these emerging materials, bamboo has garnered considerable attention as a natural composite, distinguished by its remarkable strength-to-weight ratio and unidirectional fiber reinforcement [4].

Bamboo's appeal extends beyond its mechanical properties to encompass its environmental credentials: rapid growth cycles, minimal carbon footprint, and inherent sustainability. Historically, raw bamboo has served as a construction material across diverse global contexts. However, the transition from traditional low-rise structures to modern complex buildings has been impeded by several inherent limitations: non-uniform cross-sectional geometries, the complexity of connections designed for circular profiles, and heterogeneous vascular bundle distributions [5]. These constraints have motivated the development of engineered bamboo products, notably laminated bamboo (LB) [6,7].

LB represents a significant advancement in bamboo utilization, employing manufacturing processes—including cutting, splitting, grinding, antiseptic treatment, and hot pressing—to overcome natural variability and enhance material properties. These processing techniques yield standardized dimensions and improved performance characteristics, with tensile strength and elastic modulus parallel to grain reaching 120 MPa and 12 GPa, respectively, while maintaining low carbon emissions [8–11]. The tension and compression strength are twice as large as those of wood-based materials, and the strength-to-weight ratio is close to that of steel and much larger than that of timber [12,13]. Such properties position LB as a viable alternative to conventional timber and certain fiber-reinforced composites.

Recent developments have seen the widespread adoption of LB in structural applications, including beams, columns, slabs, and walls, supported by theoretical frameworks incorporating nonlinear constitutive relationships [14,15]. The successful construction of several landmark structures has further validated LB's potential as a mainstream building material [16,17] (Figure 1). To optimize structural efficiency, researchers have developed hybrid systems combining LB with concrete [18–20], fiber-reinforced polymers [21,22], and steel [23–25], capitalizing on LB's superior tensile properties. Additionally, novel processing strategies have been explored to minimize formaldehyde emissions [26,27].



**Figure 1.** Frame structures with LB components [16,17,28].

Despite these advances, critical challenges remain in establishing reliable design methodologies for LB structures. The material's complex microstructure, inherent heterogeneity, and multiple influencing factors complicate the determination of appropriate design values. These values, derived from statistical distributions and reliability indices, must account for load duration effects, size variations, and manufacturing tolerances. Understanding the mechanisms governing these influences is therefore paramount for advancing LB structural design.

A particularly significant challenge is the size effect—the phenomenon whereby larger members exhibit lower failure stresses than smaller specimens. This behavior, observed across diverse materials including concrete [29,30] and timber [31–33], is typically addressed through dimensional restrictions in testing protocols and size-adjustment factors in design codes. For LB, a cellular and laminated material with inherent and

manufacturing-induced defects, size effects are particularly pronounced [8,34], yet remain inadequately characterized.

Various theoretical frameworks have been proposed to explain size effects in materials. The weakest-link theory, based on Weibull's statistical model, has been applied to wood-based materials [32,35,36], postulating that larger structures contain more defects, thereby increasing failure probability. However, this approach assumes series-connected elements with linear behavior, raising questions about its applicability to LB. Furthermore, while the weakest-link theory fundamentally addresses brittle failure, LB exhibits elastic–plastic behavior with quasi-brittle characteristics, arising from resin content, inherent defects, and fiber bridging mechanisms [37,38]. This creates apparent brittleness during fiber fracture while maintaining underlying ductile mechanisms.

Alternative approaches based on fracture mechanics may better capture LB's behavior. Bažant's size effect model, emphasizing fracture process zones and energy dissipation, predicts increased ductility in smaller specimens and enhanced brittleness at larger scales. This framework has demonstrated applicability to quasi-brittle materials [39–41]. Additionally, Carpinteri's multifractal theory addresses size effects through material disorder and fracture stochasticity [42–44]. Complementary analytical approaches—including regression analysis, reliability theory, cohesive models, gene expression programming, and discrete element methods—have provided valuable insights [36,45–48]. However, LB's pronounced orthotropic behavior and density variations necessitate further investigation of size-dependent failure modes and mechanical properties.

The practical implications of size effects extend to standardization challenges. Unlike concrete, timber products are governed by country-specific standards—including NDS [49], CSA O86 [50], AS 1720.1 [51], and GB 50005 [52]—each prescribing distinct methodologies, dimensions, and configurations. This diversity complicates cross-standard comparisons and international material adoption, often requiring re-evaluation under local protocols. Standardized testing procedures further illustrate these discrepancies: ASTM D143 [53] specifies small clear specimens of 25 mm × 25 mm × 100 mm or 50 mm × 50 mm × 200 mm, while GB/T 1927.11 [54] provides no dimensional specifications.

This study addresses these knowledge gaps by systematically investigating size effects on LB's compressive performance. Four specimen groups of varying dimensions were tested to evaluate length and volume influences on failure mechanisms and mechanical properties. The analysis employs Weibull's statistical theory, Bažant's fracture energy model, and Carpinteri's multifractal scaling law to interpret experimental observations and develop predictive methodologies. The role of density in modulating size effects was also examined to enhance prediction accuracy. The investigation culminates in two novel approaches, one based on discrete material attributes and another incorporating density-mechanical property relationships. These methodologies enable scholars to make accurate strength predictions, characterize size effect laws, and quantify strength degradation with increasing specimen dimensions.

The complexity of size effects in laminated bamboo arises from the interplay between multiple competing mechanisms. Unlike homogeneous materials where size effects primarily result from statistical defect distributions, LB exhibits coupled effects involving (i) adhesive interface density that increases with size, providing more potential failure initiation sites; (ii) individual strip slenderness that affects local buckling susceptibility; (iii) material heterogeneity, reflected in density variations that may amplify mechanical property gradients; and (iv) fracture process zone characteristics that govern energy dissipation during failure. Understanding these mechanisms requires not only empirical characterization but also theoretical frameworks capable of capturing the transition from ductile

to brittle behavior with increasing size. This study addresses these challenges through a comprehensive experimental program coupled with multi-model theoretical analysis.

## 2. Materials and Methods

### *2.1. Material Preparation and Processing*

#### 2.1.1. Raw Material Sourcing

The laminated bamboo (LB) specimens were manufactured from four-year-old *Phyllostachys edulis* (Moso bamboo) harvested from certified plantations in Jiangxi Province, China. The selection of four-year-old culms ensured optimal mechanical properties and fiber maturity. Following harvest, the bamboo culms underwent initial processing to produce segments ranging from 1.0 to 2.0 m in length through systematic cutting, classification, and screening procedures.

#### 2.1.2. Manufacturing Process

The LB manufacturing process comprised the following sequential operations:

Step I—Strip Preparation: Bamboo segments were split radially into uniform strips, followed by mechanical grinding to remove internodes and outer cortex layers, ensuring dimensional consistency and surface quality.

Step II—Chemical Treatment: The prepared strips underwent immersion in an antiseptic solution to enhance biological resistance against mold and insect infestation.

Step III—Moisture Conditioning: Treated strips were kiln-dried at 80 °C to achieve a target moisture content of 11% (±1%), optimizing dimensional stability and durability while preventing biological degradation.

Step IV—Resin Application and Lamination: Phenolic resin was uniformly applied to the bamboo strips using controlled coating procedures. The strips were then arranged according to predetermined layup configurations to achieve the desired thickness and mechanical properties.

Step V—Hot-Pressing Consolidation: The assembled laminates underwent hot-pressing at a temperature of 80–100 °C and pressure of 15–20 MPa for 7–10 min. These conditions facilitated resin flow and polymerization, ensuring complete interfacial bonding and void elimination between adjacent strips.

The manufacturing sequence is schematically illustrated in Figure 2. All specimens were subsequently machined to final dimensions by the Jiangxi Feiyu Bamboo Company using precision cutting equipment to ensure dimensional accuracy and surface finish.

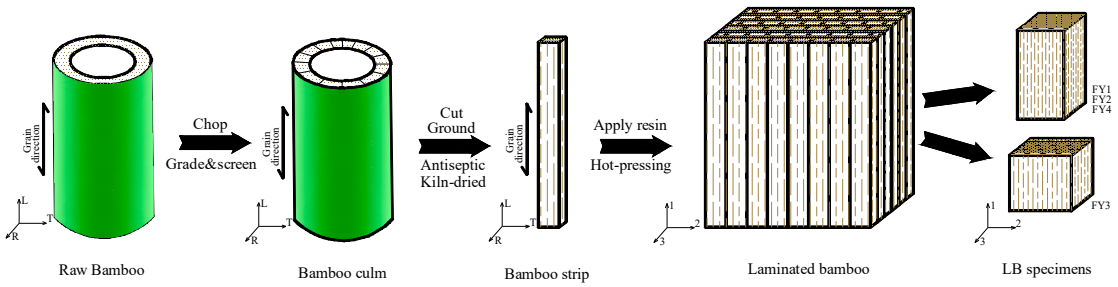



**Figure 2.** Manufacture processes of LB.

### *2.2. Specimen Design and Grouping*

#### 2.2.1. Specimen Geometry

Four distinct specimen groups were designed to investigate size effects systematically, as detailed in Table 1 and illustrated in Figure 3. The specimen configurations were selected to examine (i) proportional scaling effects, with groups FY1, FY2, and FY4

maintaining a constant aspect ratio (length-to-width ratio of 4:1) while varying in absolute dimensions, and (ii) aspect ratio effects, with groups FY2 and FY3 sharing identical cross-sectional dimensions but differing in length, enabling comparison between prismatic and cubic geometries.

**Table 1.** Specimen dimensions and grouping.

| Group | Width, *b* (mm) | Thickness, *t* (mm) | Length, *l* (mm) | Aspect Ratio (*l*/*b*) | Volume ($\times 10^3$ mm$^3$) | Sample Size |
|---|---|---|---|---|---|---|
| FY1 | 25 | 25 | 100 | 4.0 | 62.5 | 20 |
| FY2 | 50 | 50 | 200 | 4.0 | 500 | 20 |
| FY3 | 50 | 50 | 50 | 1.0 | 125 | 20 |
| FY4 | 100 | 100 | 400 | 4.0 | 4000 | 20 |

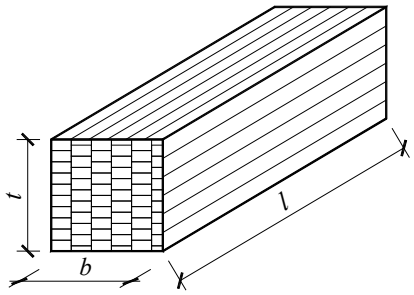



**Figure 3.** Sample dimension diagram.

2.2.2. Material Characterization

Prior to mechanical testing, material density and moisture content were determined following Chinese national standards GB/T 1927.4 [55] and GB/T 1927.5 [56], respectively, with 30 specimens placed in the same compression specimen conditions, including temperature and humidity, and then oven-dried and weighed. Table 2 presents the statistical analysis of these fundamental properties across all specimen groups.

**Table 2.** Physical properties of laminated bamboo specimens.

| Property | Mean | Standard Deviation (SD) | Coefficient of Variation (COV) |
|---|---|---|---|
| Air-dry density ($\rho_{ad}$/g·cm$^{-3}$) | 0.62 | 0.040 | 6.56% |
| Oven-dry density ($\rho_{od}$/g·cm$^{-3}$) | 0.59 | 0.026 | 1.62% |
| Moisture content (%) | 9.27 | 1.62 | 17.52% |

*2.3. Mechanical Testing Protocol*

2.3.1. Testing Equipment and Setup

Uniaxial compression tests were conducted following the protocols specified in ASTM D143 [53] and GB/T 1927.11 [54]. All specimens (FY1 to FY4) were tested using the Sans CMT5105 universal testing machine. This selection was made based on the specimen sizes and the anticipated load requirements. All tests employed displacement-controlled loading at a constant rate of 2 mm/min until specimen failure. The testing configuration is shown in Figure 4.

2.3.2. Strain Measurement and Data Acquisition

Strain measurements were recorded using a TDS-530 data acquisition system. The Axial strain gauges are of dimensions (5 mm × 3 mm, 120.1 Ω, gauge factor 2.10) positioned at mid-height on each face parallel to the loading direction. Two transverse strain gauges

with identical specifications placed on adjacent faces perpendicular to the grain direction for Poisson's ratio determination.

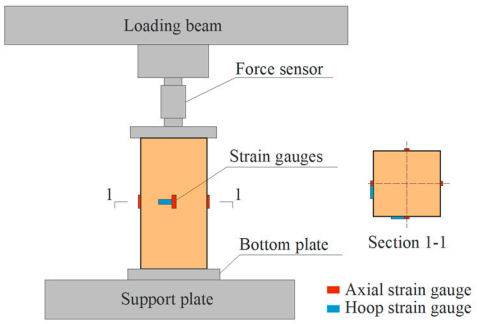



**Figure 4.** Test machine setup and strain gauge arrangement.

2.3.3. Loading Protocol and Data Analysis

The testing procedure incorporated both elastic characterization and strength determination phases. During elastic property evaluation, six complete loading–unloading cycles between 10% and 30% of the anticipated ultimate load, which was estimated with relative studies [8,57], were performed to ensure repeatable elastic response and minimize hysteresis effects. The first two cycles were excluded from analysis to account for initial settling and contact adjustment. For strength determination, monotonic loading to failure at 2 mm/min was applied, with data acquisition at 1 Hz to capture the complete load-deformation response, including post-peak behavior.

Rigorous quality control measures were implemented throughout the testing program to ensure data reliability and repeatability. Prior to testing, each specimen underwent dimensional verification with a tolerance of ±0.01 mm using digital calipers at multiple locations along the length. Moisture content was confirmed to be within the 6–8% range using a resistance-type moisture meter, with measurements taken at three locations per specimen to ensure uniformity. The parallelism of loading surfaces was verified using precision square and feeler gauges, with any deviation exceeding 0.5° requiring additional surface preparation. During testing, load eccentricity was continuously monitored through the real-time analysis of strain gauge symmetry, with tests terminated and repeated if strain differences between opposite faces exceeded 10%.

All mechanical tests were conducted under controlled environmental conditions to minimize moisture-related variability. The laboratory temperature was maintained at 23 ± 2 °C and relative humidity at 65 ± 5% throughout the testing period. Prior to testing, all specimens were conditioned in the controlled environment for a minimum of 7 days to ensure moisture equilibrium. These standardized conditions align with international testing protocols and enable direct comparison with published data for engineered bamboo products.

Mechanical properties were calculated according to the following relationships:

Compressive strength ($\sigma_c$) was calculated as follows:

$$\sigma_c = \frac{F_u}{b \cdot t} \tag{1}$$

where $F_u$ is ultimate capacity, N., and $b$, $t$ is sectional width and thickness separately, mm.

Elastic modulus ($E_c$) was determined from the final four loading–unloading cycles:

$$E_c = \frac{\Delta\sigma_c}{\Delta\varepsilon_c} \tag{2}$$

where $\Delta\sigma_c$ is changing of compressive stress, MPa. $\Delta\varepsilon_c$ is the average change in compressive strain, $\varepsilon$.

Poisson's ratio ($\nu$) was calculated using concurrent axial and transverse strain measurements:

$$\nu = -\frac{\Delta\varepsilon_2}{\Delta\varepsilon_1} \quad (3)$$

where $\Delta\varepsilon_1$ and $\Delta\varepsilon_2$ represent the strain increments parallel and perpendicular to the loading direction, respectively, measured on the same specimen face during the final four loading cycles.

## 3. Results and Discussion

### *3.1. Failure Characteristics and Mechanisms*

The compression tests revealed a consistent delamination failure mode across all specimen groups, as illustrated in Figure 5. This failure mechanism initiated through the formation of tensile cracks along the phenolic resin–bamboo interfaces, which subsequently propagated and coalesced into extended fracture planes. The observed failure pattern effectively segmented the laminated structure into multiple slender columns, leading to progressive instability and ultimate structural collapse. This delamination-dominated failure mode aligns with previous observations in laminated bamboo structures [37,38] and suggests that the adhesive interface represents the critical weak link in the composite system.



(**a**) (**b**) (**c**) (**d**)

**Figure 5.** Typical failure modes of (**a**) Group FY1, (**b**) Group FY2, (**c**) Group FY3 and (**d**) Group FY4.

A notable size-dependent variation in failure characteristics emerged from the experimental observations. Smaller specimens (FY1) exhibited narrower crack widths and enhanced resistance to crack propagation compared to larger specimens (FY4). This phenomenon can be attributed to two primary factors: first, the reduced number of adhesive interfaces in smaller specimens limits potential crack initiation sites, consistent with weakest-link theory predictions for quasi-brittle materials [58,59]; second, the lower slenderness ratios in individual bamboo strips reduce susceptibility to buckling-induced failure, a mechanism previously identified in timber composites [60,61].

The cubic specimens (FY3) demonstrated distinctly different failure characteristics compared to their prismatic counterparts. The reduced slenderness ratio minimized individual strip buckling, while four-sided lateral restraint limited global deformation, resulting in enhanced material utilization efficiency. This geometric effect on failure mode transition has been documented in other fiber-reinforced composites [62,63] and suggests that the optimization of component geometry could significantly improve structural performance.

### *3.2. Mechanical Response and Property Variations*

The stress–strain curves presented in Figure 6 reveal the characteristic mechanical response of laminated bamboo under compression. All specimens exhibited an initial linear elastic phase, followed by a nonlinear transition beyond the proportional limit, and ultimately post-peak softening behavior. This tri-linear response pattern is consistent with the behavior of other engineered bamboo products [64,65] and reflects the progressive damage accumulation in the composite microstructure.

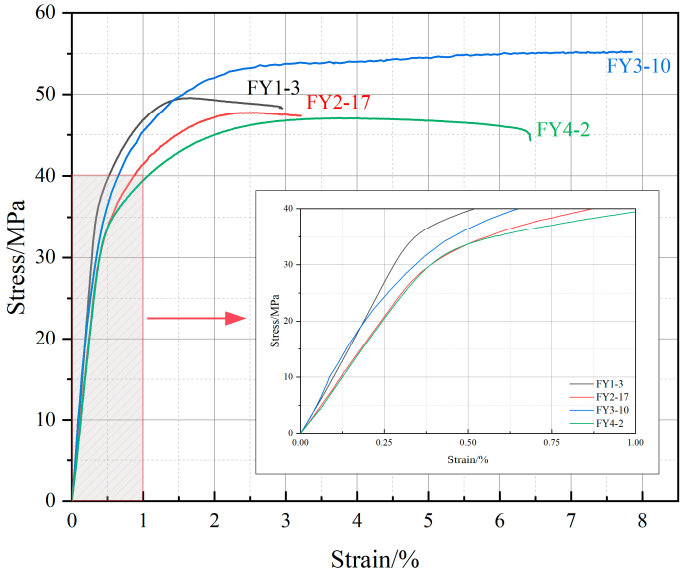



**Figure 6.** Typical stress–strain curves.

The experimental results, summarized in Table 3, reveal compressive strength values ranging from 45.65 to 55.25 MPa, representing 21.03% variation across specimen sizes. These values fall within the range reported for similar laminated bamboo products [57,66] though the observed size-dependent variation has not been previously documented. The elastic modulus showed less sensitivity to size effects, with values ranging from 8512.19 to 11,396.94 MPa, comparable to those reported by Li et al. [8] and Sharma et al. [9].

**Table 3.** Summary of mechanical properties from compression tests.

| Group | $\sigma_c$ (MPa) | $E_c$ (MPa) | $\varepsilon_c$ (%) | $\nu$ | COV$_\sigma$ (%) | COV$_E$ (%) |
|---|---|---|---|---|---|---|
| FY1 | 46.39 ± 3.92 | 9314.78 ± 578.41 | 2.19 ± 0.51 | 0.29 ± 0.04 | 8.44 | 6.21 |
| FY2 | 47.72 ± 1.25 | 9109.32 ± 542.22 | 2.18 ± 0.41 | 0.30 ± 0.07 | 2.62 | 5.95 |
| FY3 | 55.25 ± 1.09 | 11,396.94 ± 2184.32 | 3.77 ± 2.21 | 0.41 ± 0.12 | 1.97 | 19.17 |
| FY4 | 45.65 ± 0.95 | 8512.19 ± 421.16 | 2.69 ± 0.73 | 0.29 ± 0.04 | 2.07 | 4.95 |

Note: Values presented as mean ± standard deviation.

The minimal variation in mechanical properties under proportional scaling (FY1, FY2, FY4) contrasts sharply with the significant changes observed when specimen geometry was altered (FY3). The cubic specimens of FY3 exhibited 16% higher compressive strength than FY2 but with substantially increased COV$_E$ variability (19.17%), suggesting a fundamental alteration in the governing failure mechanism. This observation supports the hypothesis that the slenderness ratio plays a critical role in determining the mechanical response of laminated bamboo, similar to findings in wood composites [67,68].

### *3.3. Statistical Distribution of Mechanical Properties*

The Kolmogorov–Smirnov test results, presented in Table 4, reveal that the mechanical property distributions vary with specimen size and geometry. Groups FY2 and FY3 both exhibited preference for the Weibull distribution, while FY1 favored normal distribution and FY4 showed lognormal behavior. Notably, both Weibull-preferring groups (FY2 and FY3) represent different geometric configurations, suggesting that the statistical behavior may be influenced by both size and shape effects, rather than following a simple size-dependent pattern (Figures 7 and 8).

**Table 4.** Distribution fitting results for mechanical properties.

| Group | $D_n$ | $D_l$ | $D_w$ | $D_c$ | Optimal Distribution |
|---|---|---|---|---|---|
| FY1 | 0.118 | 0.123 | 0.131 | 0.294 | Normal |
| FY2 | 0.132 | 0.133 | 0.131 | 0.294 | Weibull |
| FY3 | 0.229 | 0.231 | 0.190 | 0.294 | Weibull |
| FY4 | 0.161 | 0.158 | 0.200 | 0.294 | Lognormal |

Note: $D_i$ = Max $\{F_o(x) - F_n(x)\}$, where $F_o(x)$ and $F_n(x)$ represent theoretical and empirical cumulative distribution functions, respectively; $D_n$: normal distribution; $D_l$: log-normal distribution; $D_w$: Weibull distribution; $D_c$: critical value ($\alpha$ = 0.05).

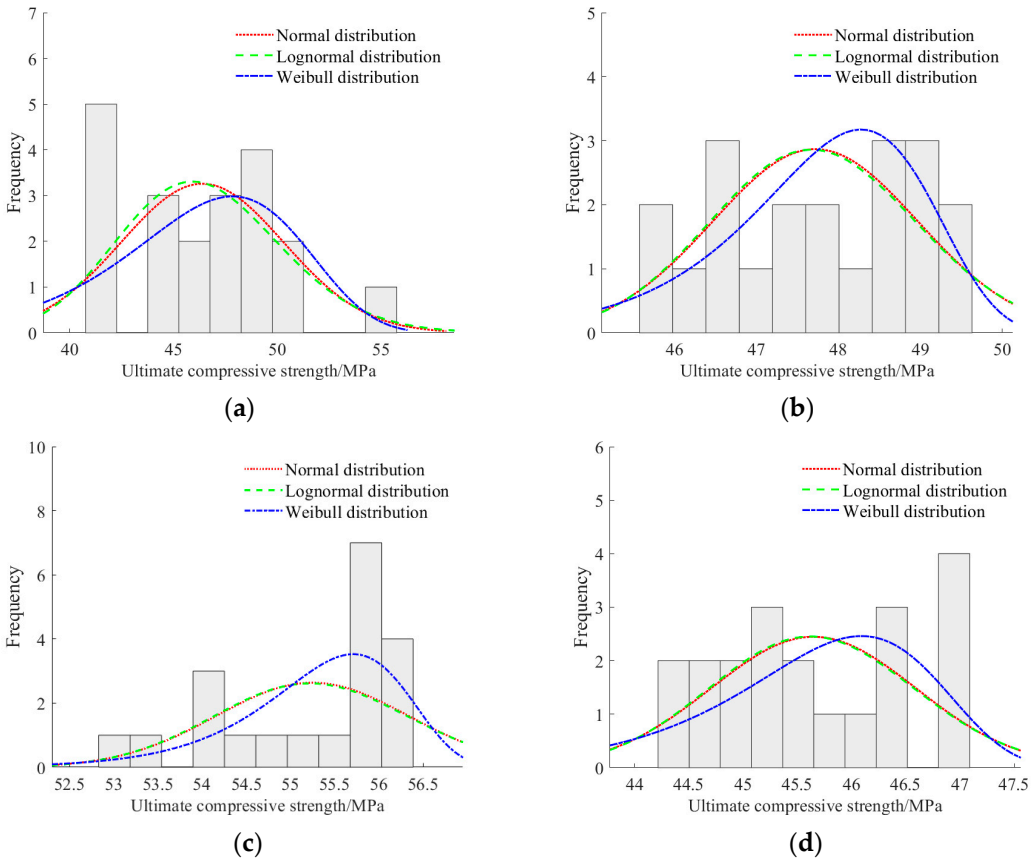



**Figure 7.** Histogram of (**a**) Group FY1, (**b**) Group FY2, (**c**) Group FY3, and (**d**) Group FY4.

The preference for Weibull distribution in certain groups aligns with weakest-link theory predictions for brittle and quasi-brittle materials [58,59]. However, the variation in optimal distributions across different sizes suggests that the size effect in laminated bamboo cannot be fully explained by a single theoretical framework, necessitating a more comprehensive modeling approach.

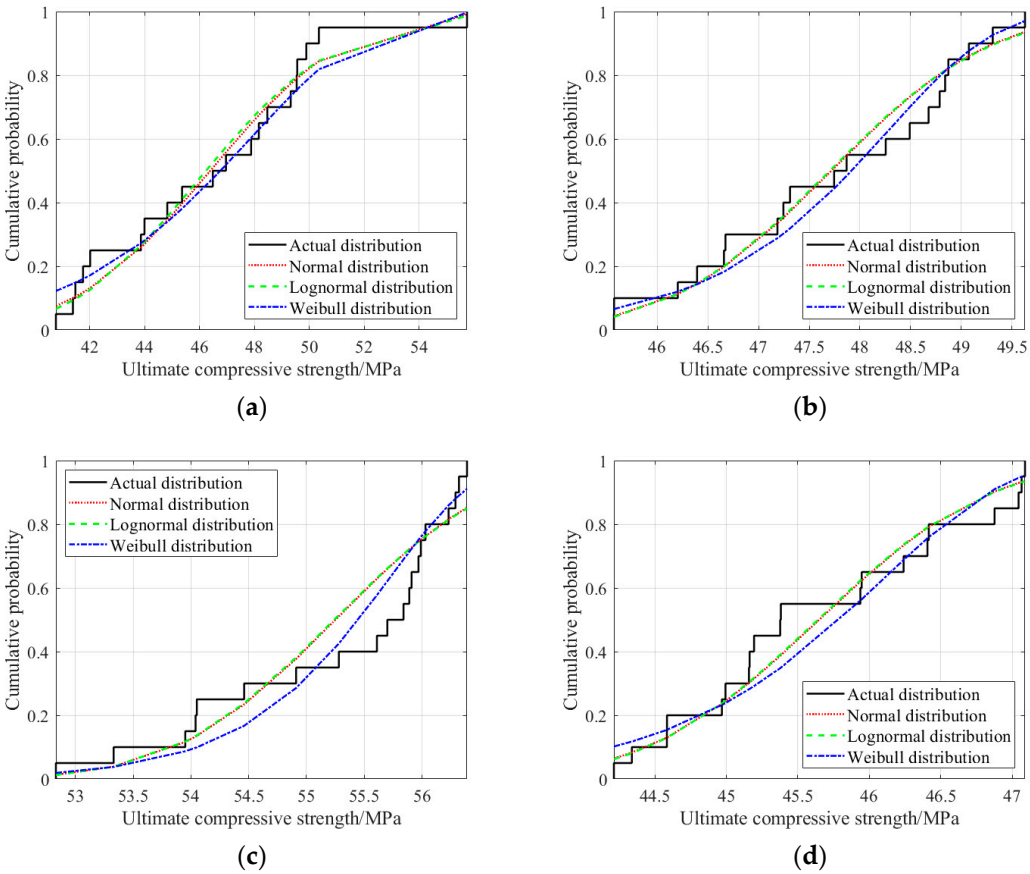



**Figure 8.** Probability cumulative curves of (**a**) Group FY1, (**b**) Group FY2, (**c**) Group FY3, and (**d**) Group FY4.

### *3.4. Quantification of Size Effects*

The analysis of the proportionally scaled specimens (FY1, FY2, FY4) revealed systematic size-dependent trends in mechanical properties, as illustrated in Figure 9. The strength exhibited an approximately linear decrease with increasing size, while the modulus showed a similar but more pronounced trend. At the largest scale tested (4× proportional scaling, corresponding to 16× cross-sectional area increase), strength and modulus reduced by 1.60% and 8.62% of the standard specimen values, respectively. This relatively modest size effect compared to concrete [69,70] and other quasi-brittle materials [71] can be attributed to the fiber-bridging mechanisms inherent in bamboo's cellular structure, which provide resistance to catastrophic crack propagation.

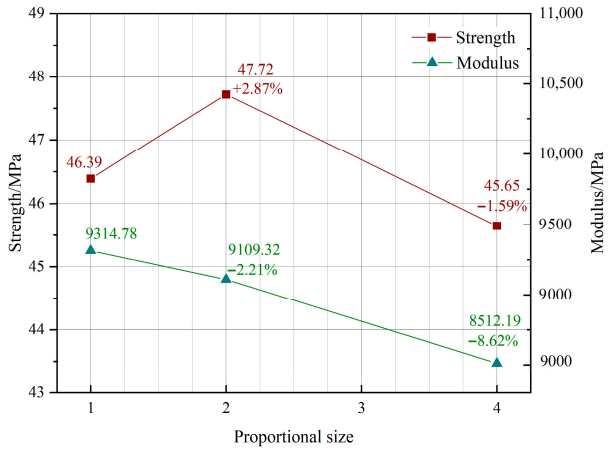



**Figure 9.** Proportional size effect.

The influence of specimen length, isolated by comparing groups FY2 and FY3, proved to be more significant than proportional scaling effects (Figure 10). The transition from prismatic to cubic geometry resulted in a 15.78% strength increases and 25.11% modulus enhancement. This substantial improvement can be attributed to the reduced susceptibility to buckling failure in shorter specimens, consistent with stability theory predictions for slender compression members. These findings align with similar observations in timber [31,33] and suggest that current design standards may be overly conservative for stocky laminated bamboo members.

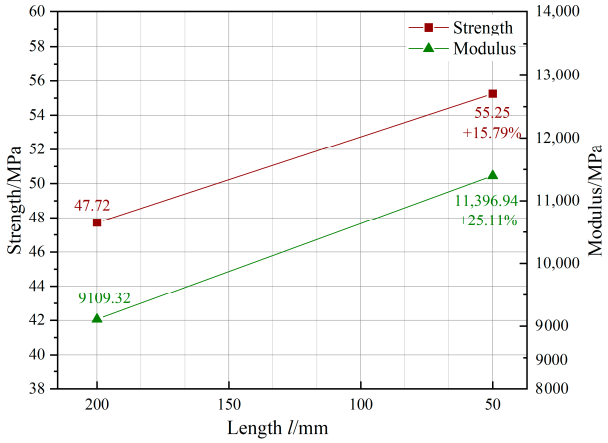



**Figure 10.** Length influence.

The observed strength increase in cubic specimens warrants detailed mechanistic explanation. The 16% strength enhancement results from three synergistic effects: (i) reduced effective length eliminates global buckling modes, allowing material strength rather than stability to govern failure; (ii) increased lateral confinement from the four-sided restraint creates a triaxial stress state that delays crack initiation; and (iii) the reduced aspect ratio changes the failure mode from progressive column instability to more uniform material crushing. This is evidenced by the higher strain at failure (3.77% vs. 2.18%) and increased Poisson's ratio (0.41 vs. 0.30) in cubic specimens, indicating enhanced lateral deformation capacity before failure.

The volume-based analysis presented in Table 5 and Figure 11 reveals non-monotonic relationships between specimen volume and mechanical properties. This complexity arises from the competing influences of absolute size (which tends to reduce strength through increased defect probability) and geometric effects (which can enhance strength through improved stability). The observed behavior cannot be adequately explained by simple volume-based weakest-link theory alone, necessitating more sophisticated modeling approaches. The non-monotonic relationship reflects the complex interplay between statistical size effects and geometric influences, with the cubic specimen (FY3) demonstrating superior performance despite its intermediate volume due to reduced slenderness effects.

**Table 5.** Volume-dependent mechanical properties.

| Group | Volume ($mm^3$) | $\sigma_c$ (MPa) | $E_c$ (MPa) | $\varepsilon_c$ (%) | $\nu$ |
|---|---|---|---|---|---|
| FY1 | 62,500.00 | 46.39 | 9314.78 | 2.19 | 0.29 |
| FY3 | 125,000.00 | 47.72 | 9109.32 | 2.18 | 0.30 |
| FY2 | 500,000.00 | 55.25 | 11,396.94 | 3.77 | 0.41 |
| FY4 | 4,000,000.00 | 45.65 | 8512.19 | 2.69 | 0.29 |

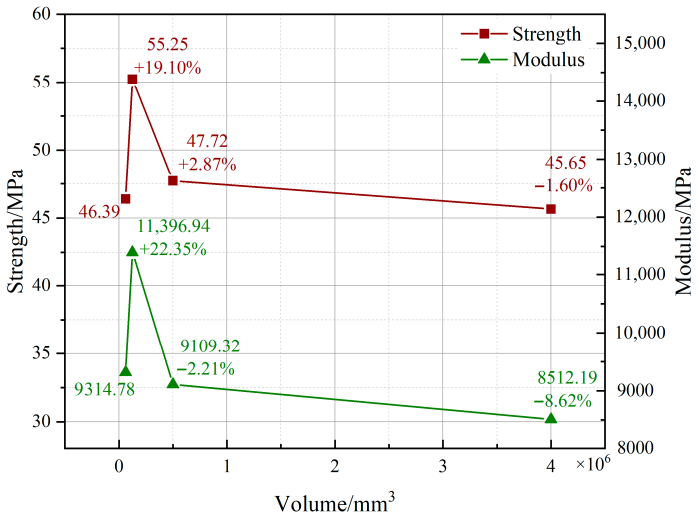



**Figure 11.** Influence of volume on strength and modulus.

### *3.5. Theoretical Modeling of Size Effects*

To characterize the observed size effects, three established theoretical frameworks were evaluated. This analysis constitutes Method 1 of our comprehensive modeling approach, which applies traditional size effect models directly to mechanical properties. Methods 2 and 3, respectively, which incorporate density effects and specific properties, will be developed in Section 3.5 based on the foundation established here.

The weakest-link model, based on Weibull statistics [35,36], assumes that failure probability increases with volume due to the higher likelihood of encountering critical defects:

$$M_{N,Wbl} = A_1 D^{-B_1} \tag{4}$$

Bažant's fracture energy model [39–41], which accounts for the energy dissipation in the fracture process zone, predicts a transition from strength-dominated to energy-dominated failure with increasing size:

$$M_{N,Fru} = B_2 f_t \cdot (1 + D/D_0)^{-1/2} \tag{5}$$

Carpinteri's multifractal scaling law [42,43,72], which considers the hierarchical nature of material disorder, provides an alternative framework:

$$M_{N,Frt} = \sqrt{A_3 + B_3/D} \tag{6}$$

where $M$ represents the mechanical property of interest, $D$ is the characteristic dimension, $f_t$ is the tensile strength (142.22 MPa), and the remaining terms are fitting parameters.

#### 3.5.1. Parameters and Estimated Values

The model fitting results for proportional scaling (Table 6) indicate that the fracture energy model best captures strength variations (SSE = 1.62), while the weakest-link model more accurately predicts modulus changes (SSE = $2.79 \times 10^4$). This dichotomy suggests that different mechanisms govern strength and stiffness size effects in laminated bamboo. The superior performance of the fracture energy model for strength prediction aligns with the quasi-brittle nature of laminated bamboo failure, where energy dissipation through fiber bridging and interface debonding plays a crucial role [38].

The estimated values obtained from these optimal models demonstrate good agreement with experimental results (Table 7), with individual prediction errors ranging from

0.78% to 2.14% for strength and 0.73% to 1.46% for modulus, yielding average errors of 0.03% (strength) and 0.05% (modulus) when applied to proportional scaling scenarios. This validates the effectiveness of Method 1 (traditional size effect models applied directly to mechanical properties) for proportional scaling conditions, though its applicability is limited to specimens that maintain constant aspect ratios.

**Table 6.** Model parameters for proportional size effects.

| Property | Model | Parameters | SSE |
|---|---|---|---|
| Strength | Weakest Link | $A_1 = 48.70$, $B_1 = 0.011$ | 1.93 |
| | Fracture Energy | $B_2 = 47.42$, $D_0 = 1.60 \times 10^3$ | 1.62 |
| | Multifractal | $A_3 = 2.15 \times 10^3$, $B_3 = 1.10 \times 10^3$ | 2.14 |
| Modulus | Weakest Link | $A_1 = 1.15 \times 10^4$, $B_1 = 0.064$ | $2.79 \times 10^4$ |
| | Fracture Energy | $B_2 = 8.98 \times 10^3$, $D_0 = -2.33 \times 10^8$ | $3.48 \times 10^5$ |
| | Multifractal | $A_3 = 7.03 \times 10^7$, $B_3 = 4.45 \times 10^8$ | $6.70 \times 10^4$ |

**Table 7.** Comparison of estimated and experimental values for proportional size effects (Method 1).

| Group | Strength | | | Modulus | | |
|---|---|---|---|---|---|---|
| | Estimated (MPa) | Experimental (MPa) | Error (%) | Estimated (MPa) | Experimental (MPa) | Error (%) |
| FY1 | 47.05 | 46.39 | 1.44 | 9383.12 | 9314.78 | 0.73 |
| FY2 | 46.70 | 47.72 | −2.14 | 8975.90 | 9109.32 | −1.46 |
| FY4 | 46.00 | 45.65 | 0.78 | 8586.36 | 8512.19 | 0.87 |
| Average | | | 0.03 | | | 0.05 |

### 3.5.2. Volume Size Effect Analysis

The fracture energy model emerged as optimal for both strength and modulus predictions when applied to volume-based analysis (Table 8). This convergence suggests that volume-based analysis better captures the fundamental size effect mechanisms in laminated bamboo, where failure initiates from distributed microcracks that coalesce through energy-driven propagation processes. The superior performance of the fracture energy model for both properties in volume analysis (SSE = 50.64 for strength, $3.70 \times 10^6$ for modulus) confirms the quasi-brittle nature of laminated bamboo failure mechanisms.

**Table 8.** Model parameters for volume-based size effects (Method 1).

| Property | Model | Parameters | SSE |
|---|---|---|---|
| Strength | Weakest Link | $A_1 = 48.88$, $B_1 = 2.07 \times 10^{-4}$ | 58.49 |
| | Fracture Energy | $B_2 = 49.75$, $D_0 = 2.68 \times 10^7$ | 50.64 |
| | Multifractal | $A_3 = 2377.00$, $B_3 = -8.56 \times 10^3$ | 58.48 |
| Modulus | Weakest Link | $A_1 = 1.09 \times 10^4$, $B_1 = 9.83 \times 10^{-3}$ | $4.64 \times 10^6$ |
| | Fracture Energy | $B_2 = 9.95 \times 10^3$, $D_0 = 1.37 \times 10^7$ | $3.70 \times 10^6$ |
| | Multifractal | $A_3 = 9.18 \times 10^7$, $B_3 = 7.82 \times 10^{-2}$ | $4.73 \times 10^6$ |

The volume-based fracture energy model predictions show reasonable agreement with experimental data (Table 9), though with larger errors than proportional scaling (average errors of 0.51% for strength and 0.92% for modulus) due to the increased complexity of three-dimensional effects and geometric variations, particularly the exceptional performance of the cubic specimen FY3.

**Table 9.** Comparison of estimated and experimental values for volume-based size effects (Method 1).

| Group | Strength | | | Modulus | | |
|---|---|---|---|---|---|---|
| | **Estimated (MPa)** | **Experimental (MPa)** | **Error (%)** | **Estimated (MPa)** | **Experimental (MPa)** | **Error (%)** |
| FY1 | 49.69 | 46.39 | 7.12 | 9923.31 | 9314.78 | 6.53 |
| FY2 | 49.63 | 47.72 | 4.02 | 9900.77 | 9109.32 | 8.69 |
| FY3 | 49.29 | 55.25 | −10.78 | 9768.70 | 11,396.94 | −14.29 |
| FY4 | 46.41 | 45.65 | 1.67 | 8746.66 | 8512.19 | 2.75 |
| Average | | | 0.51 | | | 0.92 |

#### 3.5.3. Physical Interpretation of Model Parameters

The superiority of the fracture energy model for predicting size effects in laminated bamboo reflects the quasi-brittle nature of the failure process. The model parameters provide physical insights:

- $D_0$ (characteristic dimension): The values of $2.68 \times 10^7$ mm$^3$ for strength and $1.37 \times 10^7$ mm$^3$ for modulus represent the transition volume below which material strength dominates and above which fracture energy governs failure. The large characteristic dimensions indicate that even our largest specimens (FY4 = $4 \times 10^6$ mm$^3$) remain well within the strength-dominated regime, explaining the relatively modest size effects observed. For comparison, the largest specimen volume represents only 15% of the characteristic dimension for strength, confirming that the tested specimens have not yet reached the transition to energy-dominated scaling.
- $B_2$ parameter: The ratio $B_2/f_t \approx 0.35$ suggests that approximately 35% of the material's tensile capacity contributes to the fracture process zone, consistent with fiber-bridging mechanisms in bio-composites.
- However, the convergence to fracture energy dominance in volume-based analysis suggests that three-dimensional effects unify these mechanisms under a common energy dissipation framework. This convergence indicates that as geometric complexity increases, energy-based approaches provide more robust descriptions of failure behavior than purely statistical models.

Limitations and Implications for Advanced Modeling: The limitations of Method 1, particularly its restriction to proportional scaling (excellent accuracy) versus complex geometries (larger errors) and inability to account for material heterogeneity effects, necessitate the development of more sophisticated approaches. The enhanced errors in volume-based analysis (0.51% and 0.92%) compared to proportional scaling (0.03% and 0.05%) demonstrate that traditional size effect models cannot adequately capture the complex interactions between size, geometry, and material heterogeneity observed in laminated bamboo, motivating the density-coupled modeling approaches presented in Section 3.5.

### *3.6. Influence of Density Variations*

#### 3.6.1. Specific Properties Analysis and Enhanced Sensitivity

As shown in Table 10, specific strength varied from 71.12 to 89.02 MPa·g$^{-1}$·cm$^3$, representing 25.17% variation compared to the 21.03% variation in absolute strength. This amplification of size effects when accounting for density variations highlights the importance of considering material heterogeneity in size effect analysis, a factor often overlooked in previous studies of engineered bamboo products.

The apparent paradox of density effects—where density variations are minimal (COV < 10%) yet density-coupled models dramatically improve accuracy—reveals a subtle but important mechanism. Density variations in laminated bamboo do not directly cause size effects but rather serve as indicators of local material quality and adhesive distribution. Higher density regions typically contain better-compacted fibers and more complete resin

infiltration, creating localized zones of enhanced properties. As specimen size increases, the probability of encountering low-density defect clusters increases nonlinearly, amplifying the apparent size effect.

**Table 10.** Density-normalized mechanical properties.

| Group | $\rho$ (g/cm$^3$) | Specific Strength (MPa·cm$^3$/g) | Specific Modulus (MPa·cm$^3$/g) |
|---|---|---|---|
| FY1 | 0.65 ± 0.03 | 71.97 ± 6.74 | 14,452.04 ± 1122.85 |
| FY2 | 0.62 ± 0.01 | 77.00 ± 1.85 | 14,706.26 ± 1002.11 |
| FY3 | 0.62 ± 0.01 | 89.02 ± 1.09 | 18,370.84 ± 3542.90 |
| FY4 | 0.64 ± 0.01 | 71.12 ± 1.61 | 13,258.92 ± 598.59 |

Figure 12 illustrates the effect of length $l$ on mechanical properties through comparison of groups FY2 and FY3, which share identical cross-sectional dimensions (50 × 50 mm) but differ in length (200 mm vs. 50 mm). The analysis demonstrates that both modulus and strength increased substantially as length diminished. Relative to the standard FY2 group, the cubic FY3 specimens exhibited strength, and modulus increases of 15.61% and 24.92%, respectively, signifying that length $l$ is a significant determinant of size effect.

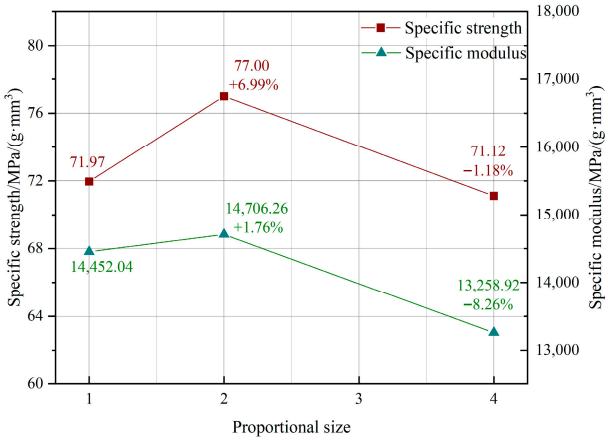



**Figure 12.** Proportional size effect on specific properties.

### 3.6.2. Single Size Effect Analysis

The results from groups FY1, FY2, and FY4 indicated that both strength and modulus diminished with the proportional increase in specimen size, as illustrated in Figure 12. The relationship between specimen size and modulus was nearly linear, although slight deviations were observed in the strength curves. When the dimensions expanded to four times the usual size (equivalent to sixteen times the standard cross-sectional area), the strength and modulus reduced by 1.18% and 8.26% of the standard specimen values, respectively. The primary cause of this decline is the increased occurrence of strips and adhesive lines, leading to defects such as bubbles in the adhesive layer, inadequate compactness, and pre-existing fractures in the original bamboo, thereby amplifying the danger of damage. Figure 13 illustrates that, when considering the influence of length $l$, specific strength exhibits a comparable tendency to the overall characteristics, characterized by a steady decrease as length increases.

The modest size effects observed in proportional scaling reflect the competing influences of statistical defect scaling (which tends to reduce properties with increasing size) and the fiber-bridging mechanisms inherent in laminated bamboo's composite structure (which provide resistance to catastrophic failure). The fracture energy model's superior performance for strength and the weakest-link model's effectiveness for modulus suggest that strength reduction involves energy-dissipative crack propagation processes, while

modulus degradation follows statistical patterns of accumulated micro-damage throughout the specimen volume.

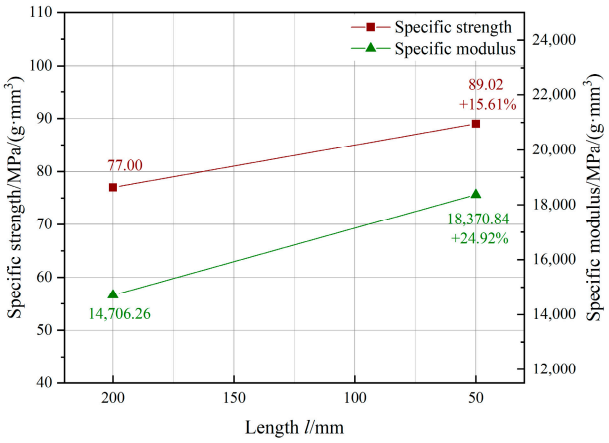



**Figure 13.** Length *l* influence on specific properties.

This finding indicates that the aspect ratio of specimens plays a crucial role in determining mechanical performance, with shorter specimens demonstrating enhanced load-bearing capacity due to several synergistic effects: (i) reduced susceptibility to buckling failure modes, allowing material strength rather than stability to govern ultimate capacity; (ii) enhanced lateral confinement effects creating beneficial triaxial stress states; and (iii) a reduced probability of encountering critical defects along the loading path. The magnitude of length effects (15.61% and 24.92%) substantially exceeds the proportional size effects (1.18% and 8.26%), demonstrating that geometric optimization provides greater performance benefits than simple size minimization.

#### 3.6.3. Model Development and Comparison

Building upon Method 1 established in Section 3.4, which demonstrated excellent accuracy for proportional scaling but limited applicability, the analysis of specific properties (normalized by density) revealed enhanced sensitivity to size effects compared to absolute mechanical properties. Two advanced modeling methods were developed to overcome Method 1's limitations:

Method 2: The application of traditional models to specific properties (strength/density, modulus/density) using modified equations:

$$m_{N,Wbl} = A_1 D^{-B_1} \tag{7}$$

$$m_{N,Fru} = B_2 f_t \cdot (1 + D/D_0)^{-1/2} \tag{8}$$

$$m_{N,Frt} = \sqrt{A_3 + B_3/D} \tag{9}$$

where $m$ is the mechanical properties which could be specific compressive modulus, specific compressive strength. Other parameters are the same as in Equations (4)–(6).

Method 3: The incorporation of density as an explicit variable in size effect relationships:

$$M_{N,Wbl} = A_1 D^{-B_1} \cdot \rho \tag{10}$$

$$M_{N,Fru} = B_2 f_t \cdot (1 + D/D_0)^{-1/2} \cdot \rho \tag{11}$$

$$M_{N,Frt} = \sqrt{A_3 + B_3/D} \cdot \rho \tag{12}$$

where $\rho$ is the average air-dry density of each group of valid data.

The progression from Method 1 (Section 3.4) through Methods 2 and 3 reflects increasing sophistication in accounting for material heterogeneity effects, with each model expanding the scope of applicability while improving prediction accuracy for complex geometric and density variations.

#### 3.6.4. Model Parameters and Validation

The model parameters for Method 2 (specific properties) are presented in Table 11, showing that the fracture energy model again provides the best fit for both specific strength and specific modulus, maintaining consistency with the volume-based analysis results.

**Table 11.** Model parameters for Method 2 (specific properties).

| Property | Model | Parameters | SSE |
|---|---|---|---|
| Specific Strength | Weakest Link | $A_1 = 78.94$, $B_1 = 1.67 \times 10^{-3}$ | 203.90 |
| | Fracture Energy | $B_2 = 79.28$, $D_0 = 2.07 \times 10^7$ | 172.10 |
| | Multifractal | $A_3 = 5.97 \times 10^3$, $B_3 = -3.58 \times 10^4$ | 204.00 |
| Specific Modulus | Weakest Link | $A_1 = 0.58$, $B_1 = 0.43$ | $9.38 \times 10^8$ |
| | Fracture Energy | $B_2 = 1.59 \times 10^4$, $D_0 = 1.18 \times 10^7$ | $1.13 \times 10^7$ |
| | Multifractal | $A_3 = 2.31 \times 10^8$, $B_3 = 0.18$ | $1.46 \times 10^7$ |

Method 3 parameters (density-coupled) are shown in Table 12, demonstrating the evolution toward more sophisticated modeling approaches that explicitly account for material heterogeneity.

**Table 12.** Model parameters for Method 3 (density-coupled).

| Property | Model | Parameters | SSE |
|---|---|---|---|
| Strength | Weakest Link | $A_1 = 76.64$, $B_1 = -3.30 \times 10^{-4}$ | 82.97 |
| | Fracture Energy | $B_2 = 78.80$, $D_0 = 2.30 \times 10^7$ | 72.31 |
| | Multifractal | $A_3 = 5.92 \times 10^3$, $B_3 = 0.26$ | 82.97 |
| Modulus | Weakest Link | $A_1 = 1.70 \times 10^4$, $B_1 = 9.27 \times 10^{-3}$ | $5.69 \times 10^6$ |
| | Fracture Energy | $B_2 = 1.58 \times 10^4$, $D_0 = 1.25 \times 10^7$ | $4.56 \times 10^6$ |
| | Multifractal | $A_3 = 2.29 \times 10^8$, $B_3 = 0.26$ | $5.78 \times 10^6$ |

The comparative analysis of prediction accuracy revealed significant differences between methods. The validation results for Method 2 are presented in Table 13, showing broader applicability than Method 1 but with increased prediction errors due to the additional complexity of density normalization.

**Table 13.** Comparison of estimated and experimental values for Method 2.

| Group | Estimated Specific Strength ($MPa \cdot g^{-1} \cdot cm^3$) | Strength | | | Estimated Specific Modulus ($MPa \cdot g^{-1} \cdot cm^3$) | Modulus | | |
|---|---|---|---|---|---|---|---|---|
| | | Estimated (MPa) | Experimental (MPa) | Error (%) | | Estimated (MPa) | Experimental (MPa) | Error (%) |
| FY1 | 79.16 | 51.12 | 46.39 | 10.20 | 15,808.05 | 10,208.51 | 9314.78 | 9.59 |
| FY2 | 79.04 | 48.99 | 47.72 | 2.67 | 15,766.43 | 9772.70 | 9109.32 | 7.28 |
| FY3 | 78.34 | 48.62 | 55.25 | −12.00 | 15,523.43 | 9635.09 | 11,396.94 | −15.46 |
| FY4 | 72.57 | 46.59 | 45.65 | 2.05 | 13,691.62 | 8789.70 | 8512.19 | 3.26 |
| Average | | | | 0.73 | | | | 1.17 |

The superior performance of Method 3 is demonstrated in Table 14, which shows the most accurate predictions across all specimen groups. This method achieves optimal balance between accuracy and general applicability by explicitly incorporating density effects while maintaining theoretical rigor.

**Table 14.** Prediction accuracy comparison for Method 3.

| Group | Strength | | | Modulus | | |
|---|---|---|---|---|---|---|
| | Estimated (MPa) | Experimental (MPa) | Error (%) | Estimated (MPa) | Experimental (MPa) | Error (%) |
| FY1 | 50.82 | 46.39 | 9.55 | 10,145.77 | 9314.78 | 8.92 |
| FY2 | 48.71 | 47.72 | 2.08 | 9714.22 | 9109.32 | 6.64 |
| FY3 | 48.39 | 55.25 | −12.42 | 9586.46 | 11,396.94 | −15.89 |
| FY4 | 46.69 | 45.65 | 2.28 | 8804.02 | 8512.19 | 3.43 |
| Average | | | 0.37 | | | 0.78 |

The systematic improvement in prediction accuracy demonstrates evolution from the following methods:

- Method 1 (Section 3.4): Average errors of 0.03% (strength) and 0.05% (modulus) for proportional scaling, demonstrating good accuracy but limited to constant aspect ratios.
- Method 2: Average errors of 0.73% (strength) and 1.17% (modulus) for specific properties, with broader applicability to geometric variations.
- Method 3: Average errors of 0.37% (strength) and 0.78% (modulus) for density-coupled analysis, providing optimal balance between accuracy and general applicability across all specimen configurations.

#### 3.6.5. Limitations and Validity Range

The applicability of the developed size effect models is constrained by several factors inherent to experimental design and material characteristics. Geometrically, the models have been validated for aspect ratios ranging from 1:1 to 4:1, representing the transition from cubic to slender prismatic members. Extrapolation beyond these limits, particularly to very slender members with aspect ratios exceeding 4:1 or to plate-like geometries, requires additional validation as different failure mechanisms may become dominant. The tested volume range spans from 62,500 $mm^3$ to 4,000,000 $mm^3$, encompassing typical laboratory to small structural member scales. However, full-scale structural elements often exceed these dimensions, and the assumption of consistent size effect behavior at larger scales remains unverified.

The loading conditions in this study were limited to monotonic uniaxial compression applied at a constant displacement rate. Real structural applications involve complex stress states, including combined axial–flexural loading, cyclic loading, and long-term sustained loads. The interaction between size effects and these alternative loading conditions requires separate investigation, as the governing failure mechanisms may differ substantially from those observed under simple compression. Additionally, the material scope only encompasses Moso bamboo (Phyllostachys edulis), which is processed using standard lamination techniques with phenolic resin adhesive. Different bamboo species exhibit varying fiber densities and mechanical properties, while alternative adhesive systems and processing parameters may significantly influence the magnitude and nature of size effects.

Environmental factors represent another critical limitation of the current models. All testing was conducted under standard laboratory conditions (23 °C, 65% RH) with equilibrium moisture content around 6–8%. In service conditions, laminated bamboo experiences fluctuating temperature and humidity, leading to moisture gradients, differential swelling, and the potential degradation of adhesive bonds. These effects may interact with size in complex ways, as larger members experience greater moisture gradients and longer equilibration times. Furthermore, the models do not account for time-dependent phenomena such as creep, stress relaxation, or long-term material degradation, all of which may exhibit their own size dependencies. Future research should address these limitations through

expanded testing programs and refined theoretical frameworks to enable the confident application of laminated bamboo in diverse structural contexts.

### *3.7. Critical Dimensions and Design Implications*

The practical application of these findings requires the establishment of size effect factors for design purposes. Using the standard specimen dimensions (25 × 25 × 100 mm) as reference and applying the optimal modeling approach (Method 3), size effect factors were calculated across a range of component dimensions (Figure 14). The analysis reveals an exponential decay pattern, with rapid initial reduction followed by asymptotic stabilization at larger sizes.

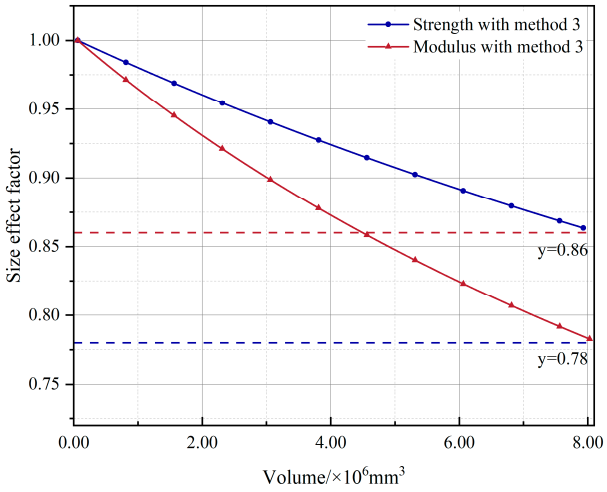



**Figure 14.** Factor–size curves based on volume.

The critical dimensions beyond which size effects stabilize were determined as 125.64 mm for strength and 126.14 mm for modulus (Table 15), corresponding to size effect factors of 0.86 and 0.78, respectively. These values are less severe than those reported for unreinforced concrete [73,74] but more significant than those for fiber-reinforced polymer composites [75,76], reflecting the intermediate nature of laminated bamboo as a bio-composite material.

**Table 15.** Design size effect factors.

| Property | Size Effect Factor | Critical Volume ($mm^3$) | Critical Side Length (mm) * |
|---|---|---|---|
| Strength | 0.86 | 7,932,500.00 | 125.64 |
| Modulus | 0.78 | 8,027,500.00 | 126.14 |

* For square cross-section with length-to-width ratio of 4:1.

These findings have important implications for the structural design of laminated bamboo components. Current design standards [77] do not explicitly account for size effects in laminated bamboo, potentially leading to unconservative designs for large-scale applications. The established size effect factors provide a rational basis for modifying design values based on component dimensions, enhancing both safety and efficiency in structural applications. Furthermore, the identification of delamination as the primary failure mode suggests that improvements in adhesive technology and manufacturing processes could significantly mitigate size effects, opening possibilities for larger-scale bamboo construction without proportional strength penalties.

## 4. Conclusions

This comprehensive investigation of size effects in laminated bamboo under compression advances both fundamental understanding and practical design capabilities for this sustainable construction material. The key findings and their implications are as follows:

1. Traditional size effect models (Method 1) demonstrate good accuracy for proportional scaling but limited scope. While proportional scaling produces modest mechanical property reductions (60% strength, 8.62% modulus for 4× scaling), the fracture energy model's superior performance confirms that quasi-brittle fracture mechanics, rather than simple statistical effects, govern the scaling behavior.
2. The significant influence of length effects (15.78% strength increase, 25.11% modulus increase with reduced length) demonstrates that optimizing component geometry offers more substantial improvements than simply minimizing overall size. This finding suggests that current design practices favoring slender members may be unnecessarily conservative, and that stockier cross-sections could enable more efficient material utilization.
3. The systematic progression from Method 1 (excellent accuracy for proportional scaling but limited scope) through Method 2 (0.73–1.17% errors, broader applicability to geometric variations) to Method 3 (0.37–0.78% errors, optimal performance across all configurations) demonstrates that incorporating density effects captures material heterogeneity that amplifies size-dependent behavior. Despite minimal air-dry density variations (COV = 9.27%), density-coupled models reveal that local material quality indicators scale nonlinearly with volume, providing order-of-magnitude improvements in prediction accuracy for complex geometries.
4. The identified threshold dimensions of 125.64 mm (strength) and 126.14 mm (modulus) for square sections with 4:1 aspect ratios provide practical design boundaries. Components exceeding these dimensions can use constant reduction factors (0.86 for strength, 0.78 for modulus) rather than size-dependent adjustments, simplifying design procedures while maintaining safety. These values position laminated bamboo between unreinforced concrete (more severe effects) and FRP composites (less severe effects) in the materials hierarchy.
5. The consistent delamination failure mode across all specimen sizes indicates that advances in bio-based adhesive technology could substantially reduce size effects. Enhanced interfacial bonding would not only increase absolute strength but also reduce sensitivity to scale, enabling larger structural applications without proportional property penalties and potentially shifting the critical dimensions to larger values.

These findings provide the quantitative foundation necessary for incorporating laminated bamboo into modern structural design codes while addressing the current gap where existing standards fail to account for size effects. The established size effect factors offer immediate practical value for structural engineers, while the identified mechanisms point toward specific technological developments needed to expand bamboo's application envelope.

Future investigations should extend this framework to other loading conditions (flexural, tensile, combined stress states), environmental exposures (moisture, temperature, long-term effects), and hybrid structural systems to fully realize bamboo's potential as a sustainable alternative to conventional construction materials. The demonstrated success of density-coupled modeling approaches also suggests opportunities for developing advanced quality control methods based on non-destructive density measurements during manufacturing.

**Author Contributions:** Conceptualization, J.-N.L.; Methodology, A.S. and J.-W.Z.; Investigation, A.S., J.-W.Z., H.-T.Z. and Y.-C.L.; Data curation, H.-T.Z. and Y.-C.L.; Writing—original draft, J.-N.L. and A.S.; Writing—review & editing, J.-N.L. and A.S.; Funding acquisition, A.S. and J.-W.Z. All authors have read and agreed to the published version of the manuscript.

**Funding:** This research was funded by the Natural Science Foundation of Jiangsu Educational Department (No. 23KJA560003); Changzhou Sci & Tech Program (No. CQ20214030); Jiangsu Province Innovation Training Project (No. 202511055109Y, No. 202511055110Y).

**Data Availability Statement:** Data will be made available on request.

**Conflicts of Interest:** The authors declare no conflicts of interest.

## References

1. Liu, C.; Yue, S.; Zhou, C.; Sun, H.; Deng, S.; Gao, F.; Tan, Y. Anisotropic mechanical properties of extrusion-based 3D printed layered concrete. *J. Mater. Sci.* **2021**, *56*, 16851–16864. [CrossRef]
2. Li, J.n.; Singh, A.; Zhao, Y.; Sun, J.; Tam, V.W.Y.; Xiao, J. Enhancing thermo-mechanical and moisture properties of 3D-Printed concrete through recycled ultra-fine waste glass powder. *J. Clean. Prod.* **2024**, *480*, 144121. [CrossRef]
3. Singh, A.; Miao, X.; Zhou, X.; Deng, Q.; Li, J.; Zou, S.; Duan, Z. Use of recycled fine aggregates and recycled powders in sustainable recycled concrete. *J. Build. Eng.* **2023**, *77*, 107370. [CrossRef]
4. Chen, X.; Wang, X.; Luo, X.; Chen, L.; Li, Y.; Xu, J.; Liu, Z.; Dai, C.; Miao, H.; Liu, H. Bamboo as a natural optimized fiber reinforced composite: Interfacial mechanical properties and failure mechanisms. *Compos. Part B Eng.* **2024**, *279*, 111458. [CrossRef]
5. Akinbade, Y.; Harries, K.A.; Sharma, B.; Ramage, M.H. Variation of through-culm wall morphology in P. edulis bamboo strips used in glue-laminated bamboo beams. *Constr. Build. Mater.* **2020**, *232*, 117248. [CrossRef]
6. Li, L.; Huang, C.; Guo, N. Flexural behaviour of bamboo scrimber beams with different composite and reinforced technology: A literature review. *Case Stud. Constr. Mater.* **2024**, *20*, e02805. [CrossRef]
7. Chen, L.; Luo, X.; Huang, B.; Ma, Y.; Fang, C.; Liu, H.; Fei, B. Properties and bonding interface characteristics of an innovative bamboo flattening and grooving unit (BFGU) for laminated bamboo lumber. *Colloids Surf. A Physicochem. Eng. Asp.* **2023**, *676*, 132185. [CrossRef]
8. Li, J.; Yan, J.; Zhou, Y.; Yang, S.; Singh, A. Analyzing the effects of size and density on the ultimate compressive strength of structural laminated bamboo parallel to the grain. *J. Build. Eng.* **2024**, *90*, 109481. [CrossRef]
9. Li, J.; Singh, A.; Sharma, R.; Yu, X.; Zhou, J.; Ge, P.; Yang, S. Size Influence of Laminated Bamboo on Tensile Mechanical Properties with the Consideration of Density. *Materials* **2025**, *18*, 238. [CrossRef]
10. Liu, K.; Jayaraman, D.; Shi, Y.; Xiong, Z.; Yang, J.; Symeonidis, A.; Escamilla, E.Z. Life cycle assessment (LCA) of the industrial production of structural glued laminated bamboo. *J. Clean. Prod.* **2024**, *485*, 144367. [CrossRef]
11. Li, J.; Singh, A.; Yu, X.; Zhou, J.; Ge, P.; Yang, S. Size influence of laminated bamboo bending mechanical properties with the consideration of density. *J. Build. Eng.* **2025**, *111*, 113489. [CrossRef]
12. Mashrah, W.A.H.; Boufendassa, R.; Fu, X.; Al-Mansour, A.; Yu, Y.; Amer, M.; Mo, S. Comprehensive review of engineered bamboo in structural engineering: Comparative insights into laminated bamboo and bamboo scrimber. *Structures* **2025**, *76*, 108896. [CrossRef]
13. Dauletbek, A.; Li, H.; Lorenzo, R.; Corbi, I.; Corbi, O.; Ashraf, M. A review of basic mechanical behavior of laminated bamboo lumber. *J. Renew. Mater.* **2021**, *10*, 273–300. [CrossRef]
14. Li, J.; Singh, A.; Zhou, Y. Experimental study on the flexural behavior of I-shaped laminated bamboo composite beam as sustainable structural element. *Buildings* **2024**, *14*, 671. [CrossRef]
15. Su, Y.; Zou, J.; Lu, W. A macroscopic shear angle model for ultimate bearing capacity of glued laminated bamboo hollow columns under axial compression. *Structures* **2022**, *45*, 560–571. [CrossRef]
16. Li, H.; Xue, X.; Xiong, Z.; Ashraf, M.; Lorenzo, R.; Shuchi, S. Application case of laminated bamboo lumber structure—Building of Sentai Bamboo Research Center. *Sustain. Struct.* **2024**, *4*, 000043. [CrossRef]
17. Huang, D.; Zhu, J.; Shen, Y. Design of a 3-storey frame building using engineered bamboo composite (EBC). *Eng. Struct.* **2024**, *300*, 117230. [CrossRef]
18. Deng, Y.; Hao, Y.; Mohamed, A.; Wong, S.H.F.; Tang, Y.; Yuen, T.Y.P.; Sukontasukkul, P.; Shen, M.; Fernando, N.; Saint, R.; et al. Experimental investigation of mechanically laminated straight or curved-and-tapered bamboo-concrete T-beams. *Eng. Struct.* **2023**, *283*, 115896. [CrossRef]
19. Zhang, Z.; Wei, Y.; Yi, J.; Wei, B.; Lin, Y.; Huang, S. Experiments and design of laminated bamboo and concrete-filled steel tube columns under axial compression. *Eng. Struct.* **2024**, *318*, 118692. [CrossRef]

20. Du, H.; Xu, R.; Liu, P.; Yuan, S.; Wei, Y. Experimental and theoretical evaluation of inclined screws in glued laminated bamboo and timber-concrete composite beams. *J. Build. Eng.* **2024**, *91*, 109579. [CrossRef]
21. Wang, Z.; Li, H.; Fei, B.; Ashraf, M.; Xiong, Z.; Lorenzo, R.; Fang, C. Axial compressive performance of laminated bamboo column with aramid fiber reinforced polymer. *Compos. Struct.* **2021**, *258*, 113398. [CrossRef]
22. Zhang, H.; Lu, R.; Li, H.; Xiong, Z.; Ashraf, M. Dynamic response of fiber-reinforced polymer laminated bamboo lumber beams under cyclic loading. *Structures* **2025**, *72*, 107920. [CrossRef]
23. Tian, Y.; Li, H.; Chen, B.; Lorenzo, R.; Ashraf, M. Experimental and theoretical investigation of prestressed-steel-reinforced laminated bamboo lumber beams. *Structures* **2023**, *47*, 434–448. [CrossRef]
24. Ma, R.; Wang, X.; Du, Y.; Sun, G.; Kang, S.B.; Ma, J.; Chen, Z. Experimental and theoretical investigation into flexural performance of thin-walled steel-laminated bamboo lumber truss beam. *Thin-Walled Struct.* **2024**, *199*, 111841. [CrossRef]
25. Zhang, Z.; Wei, Y.; Yuan, Z.; Lin, Y.; Chen, J. Axial compression behavior of laminated bamboo columns restrained by rectangular steel tubes. *Eng. Struct.* **2025**, *328*, 119723. [CrossRef]
26. Zhang, Z.; Wei, Y.; Yuan, Z.; Yi, J.; Chen, S.; Chen, J. Flexural modeling and failure criteria of thermal modified laminated bamboo beams. *Constr. Build. Mater.* **2024**, *435*, 136885. [CrossRef]
27. Zhao, E.; Liu, J.; Zhang, X.; Wang, F. Eccentric compression behavior of inorganic-bonded bamboo composite columns. *Structures* **2025**, *72*, 108287. [CrossRef]
28. Dauletbek, A.; Li, H.; Xiong, Z.; Lorenzo, R. A review of mechanical behavior of structural laminated bamboo lumber. *Sustain. Struct.* **2021**, *1*, 000004. [CrossRef]
29. Ye, J.; Yang, M.; Yu, J.; Dai, Y.; Yin, B.B.; Weng, Y. Size effect on flexural and fracture behaviors of 3D printed engineered cementitious composites: Experimental and numerical studies. *Eng. Struct.* **2024**, *298*, 117062. [CrossRef]
30. Hao, Y.; Li, Y.; Guan, J.; Xie, C.; Li, L.; Chen, S.; He, S.; Wei, S. Strength size effect model of fully substituted coal gangue concrete under coupled action of sulfate attack and dry-wet cycles. *Constr. Build. Mater.* **2025**, *467*, 140313. [CrossRef]
31. Crist 'obal, T.; Simon, A. Survival analysis of tensile strength variation and simulated length-size effect along Oak boards. *J. Eng. Mech.* **2022**, *148*, 04021130. [CrossRef]
32. Wu, G.; Chen, B.; Zhong, Y.; Zhang, Y.; Ren, H.; Shen, Y. Effect of size on tensile strength parallel to grain of high-performance wood scrimber. *Constr. Build. Mater.* **2024**, *449*, 138399. [CrossRef]
33. Walley, S.M.; Rogers, S.J. Is Wood a Material? Taking the Size Effect Seriously. *Materials* **2022**, *15*, 5403. [CrossRef] [PubMed]
34. Wu, Y.; Liu, S.; Li, Z.; Xu, J.; Xu, W. Comparative study of toughness and energy evaluation of laminated bamboo composites and toughening mechanism. *Compos. Struct.* **2025**, *352*, 118706. [CrossRef]
35. Wu, G.; Zhang, Y.; Zhong, Y.; Ren, H.; Shen, Y. Size effect on the compressive strength of a novel structural wood composite: High-performance wood scrimber. *Ind. Crops Prod.* **2024**, *221*, 119381. [CrossRef]
36. Vida, C.; Lukacevic, M.; Hochreiner, G.; Füssl, J. Size effect on bending strength of glued laminated timber predicted by a numerical simulation concept including discrete cracking. *Mater. Des.* **2023**, *225*, 111550. [CrossRef]
37. Yang, D.; Li, H.; Xiong, Z.; Mimendi, L.; Lorenzo, R.; Corbi, I.; Corbi, O.; Hong, C. Mechanical properties of laminated bamboo under off-axis compression. *Compos. Part A Appl. Sci. Manuf.* **2020**, *138*, 106042. [CrossRef]
38. Liu, Y.; Sheng, B.; Huang, D.; Zhou, A. Mode-I interlaminar fracture behavior of laminated bamboo composites. *Adv. Struct. Eng.* **2021**, *24*, 733–741. [CrossRef]
39. Wang, Q.; Li, Q.; Yin, X.; Xu, S.; Su, Z.; Xie, H. Fracture behavior and size effect of UHPFRC: Experimental and meso-scale numerical investigation. *Eng. Fract. Mech.* **2023**, *283*, 109197. [CrossRef]
40. Wu, F.; Li, B.; Yu, J.; Li, Y.; Wang, S.; Jiang, G.; Wang, S. Size effect in the mechanical characteristics of steel fiber reinforced alkali-activated slag/fly ash-based concrete. *Constr. Build. Mater.* **2024**, *443*, 137827. [CrossRef]
41. De La Rosa, Á.; Ruiz, G. A new approach to the study of the size and the geometry effect on compressive strength in concrete. *Results Eng.* **2025**, *25*, 104261. [CrossRef]
42. Shu, Y.; Shen, Z.; Zhang, H.; Gan, L.; Xu, L.; Sun, Y.; Yu, J.a.; Wang, R. Size effect of tensile bonding strength between new and old concrete. *J. Build. Eng.* **2024**, *97*, 110739. [CrossRef]
43. Kosteski, L.E.; Iturrioz, I.; Lacidogna, G.; Carpinteri, A. Size effect in heterogeneous materials analyzed through a lattice discrete element method approach. *Eng. Fract. Mech.* **2020**, *232*, 107041. [CrossRef]
44. Jiang, N.; Ge, Z.; Wang, Z.; Gao, T.; Zhang, H.; Ling, Y.; Šavija, B. Size effect on compressive strength of foamed concrete: Experimental and numerical studies. *Mater. Des.* **2024**, *240*, 112841. [CrossRef]
45. De Santis, Y.; Aloisio, A.; Pasca, D.P.; Fragiacomo, M.; Dombrowski, F. Evaluation of the shear size effect in glued laminated timber using a stochastic FE model calibrated on 17000 glue-line tests. *Constr. Build. Mater.* **2023**, *399*, 132488. [CrossRef]
46. Liu, Y.; Liu, X.; Yuan, C. Improved size effect law (SEL) considering size-dependent fracture process zone (FPZ) for quasi-brittle materials. *J. Build. Eng.* **2024**, *92*, 109770. [CrossRef]
47. Ye, J.; Uddin, M.N.; Yu, J.; Xu, T.; Zhan, Y.; Zhang, D.; Weng, Y. A data-driven approach to predicting multifactor-influenced flexural size effect and fracture behaviors of concrete. *Eng. Fract. Mech.* **2025**, *315*, 110794. [CrossRef]

48. Qiu, J.; Kuang, D.M.; Wang, M.B.; Chen, L.; Peng, C.; Song, Z.B. Numerical simulation of the size effect on rock particle crushing behavior considering microscopic heterogeneous bond strength characteristics. *Soils Rocks* **2025**, *48*, e2025009723. [CrossRef]
49. NDS. *National Design Specification for Wood Construction*; American Forest and Paper Association: Washington, DC, USA, 2018.
50. Canadian Standards Association. *Engineering Design in Wood O86*; Canadian Standards Association: Toronto, ON, Canada, 2014.
51. *AS1720.1*; Timber Structures—Part 1: Design Methods. Standards Australia: Sydney, Australia, 2010.
52. *GB 50005*; Standard for Design of Timber Structures. Ministry of Housing and Urban-Rural Development of the People's Republic of China: Beijing, China, 2017.
53. *ASTM D143-14*; Standard Test Methods for Small Clear Specimens of Timber. ASTM International: West Conshohocken, PA, USA, 2014.
54. *GB/T 1927.11*; Test Methods for Physical and Mechanical Properties of Small Clear Wood Specimens-Part 11: Determination of Ultimate Stress in Compression Parallel to Grain. The Standardization Administration of the People's Republic of China: Beijing, China, 2022.
55. *GB/T 1927.4*; Test Methods for Physical and Mechanical Properties of Small Clear Wood Specimens-Part 4: Determination of Moisture Content. The Standardization Administration of the People's Republic of China: Beijing, China, 2021.
56. *GB/T 1927.5*; Test Methods for Physical and Mechanical Properties of Small Clear Wood Specimens-Part 5: Determination of Density. The Standardization Administration of the People's Republic of China: Beijing, China, 2021.
57. Tang, S.; Zhou, A.; Li, J. Mechanical properties and strength grading of engineered bamboo composites in China. *Adv. Civ. Eng.* **2021**, *2021*, 6666059. [CrossRef]
58. Wang, X.; Dong, E.; Jia, Z.; Jia, L.; Xia, K.; Zhang, Z.; Chen, Y.; Zhang, L.; Gao, Y.; Zhang, Y. Specimen size effect on compressive strength of 3D printed concrete containing coarse aggregate with varying water to binder ratios. *J. Build. Eng.* **2024**, *97*, 110704. [CrossRef]
59. Ye, J.; Yu, J.; Yu, J.; Yu, K.; Wang, Y.; Weng, Y. Tensile size effect of engineered cementitious composites (ECC): Experimental and theoretical investigations. *Constr. Build. Mater.* **2023**, *402*, 133053. [CrossRef]
60. Wei, H.; Shi, D.; Rupert, E.; Fragiacomo, M.; Demartino, C.; Xiao, Y. Axial compressive behavior of novel laminated bamboo tubes: Experimental tests and predictive buckling model. *Constr. Build. Mater.* **2025**, *463*, 139987. [CrossRef]
61. Wang, Z.; Li, H.; Xiong, Z.; Lorenzo, R.; Ashraf, M. Behavior of laminated bamboo columns under low cyclic reversed loading. *Structures* **2024**, *70*, 107671. [CrossRef]
62. Kang, T.; Li, S.; Jin, L.; Wu, X.; Zhou, J.; Zhang, Y.; Liang, Y. Size effect on compressive behaviors of waste fiber-reinforced recycled aggregate concrete. *Eur. J. Environ. Civ. Eng.* **2022**, *26*, 7811–7824. [CrossRef]
63. Fang, H.; Gu, M.; Zhang, S.; Jiang, H.; Fang, Z.; Hu, J. Effects of Steel Fiber and Specimen Geometric Dimensions on the Mechanical Properties of Ultra-High-Performance Concrete. *Materials* **2022**, *15*, 3027. [CrossRef]
64. Yang, Y.; Qiu, Z.; Yang, S.; Lin, J.; Cao, H.; Bao, W.; Fan, H. Effects of cross-section morphology, vascular bundle content and anisotropy on compression failure of laminated bamboo columns. *Eng. Fract. Mech.* **2023**, *290*, 109497. [CrossRef]
65. Yang, Y.; Yang, S.; Lin, J.; Qiu, Z.; Fan, H. Engineering fracture mechanics of laminated bamboo lumbers: Numerical and theoretical methods. *Eng. Fract. Mech.* **2025**, *321*, 111102. [CrossRef]
66. Chen, G.; Yu, Y.; Li, X.; He, B. Mechanical behavior of laminated bamboo lumber for structural application: An experimental investigation. *Eur. J. Wood Wood Prod.* **2020**, *78*, 53–63. [CrossRef]
67. Su, Y.; Zou, J. Local stability of glued laminated bamboo columns with box sections under axial compression. *Eur. J. Wood Wood Prod.* **2024**, *82*, 1171–1185. [CrossRef]
68. Zheng, Y.; Zhou, C. Effect of slenderness ratio on axial compression behavior of circular wood columns strengthened with high-performance bamboo-based composites. *Eng. Struct.* **2024**, *320*, 118910. [CrossRef]
69. Çetin, S.Y. An experimental study of basalt aggregate concrete according to different size effect laws. *Alex. Eng. J.* **2025**, *120*, 358–370. [CrossRef]
70. Zhang, Y.; Zheng, Y.; Hu, S.; Du, C. Size effect difference between uniaxial and splitting tensile strength of recycled aggregate concrete considering the maximum aggregate size: Meso-simulation. *Constr. Build. Mater.* **2025**, *462*, 139961. [CrossRef]
71. Huang, Y.; Han, J.; Sun, J.; Zhao, T. Size effects on the in-situ compressive behavior of first-year sea ice. *Appl. Ocean. Res.* **2025**, *154*, 104395. [CrossRef]
72. Anagnostopoulos, C.A.; Cabja, D.; Papadimitriou, C.A. Experimental data on strength properties of mussel shell concretes and specimen size effect. *Data Brief* **2021**, *35*, 106954. [CrossRef]
73. Bažant, Z.P. Size Effect in Blunt Fracture: Concrete, Rock, Metal. *J. Eng. Mech.* **1984**, *110*, 518–535. [CrossRef]
74. Lee, B.J.; Kee, S.H.; Oh, T.; Kim, Y.Y. Effect of Cylinder Size on the Modulus of Elasticity and Compressive Strength of Concrete from Static and Dynamic Tests. *Adv. Mater. Sci. Eng.* **2015**, *2015*, 580638. [CrossRef]
75. Liu, H.; Ka, T.A.; Su, N.; Zhu, Y.; Guan, S.; Long, J.; Tafsirojjaman, T. Experimental Study of Dimensional Effects on Tensile Strength of GFRP Bars. *Buildings* **2024**, *14*, 1205. [CrossRef]

76. Wisnom, M.R. Size effects in the testing of fibre-composite materials. *Compos. Sci. Technol.* **1999**, *59*, 1937–1957. [CrossRef]
77. *ISO 23478*; Bamboo Structures—Engineered Bamboo Products—Test Methods for Determination of Physical and Mechanical Properties. International Organization for Standardization: Geneva, Switzerland, 2022.

**Disclaimer/Publisher's Note:** The statements, opinions and data contained in all publications are solely those of the individual author(s) and contributor(s) and not of MDPI and/or the editor(s). MDPI and/or the editor(s) disclaim responsibility for any injury to people or property resulting from any ideas, methods, instructions or products referred to in the content.